Photoinduced dynamics in an exchange-coupled trinuclear iron cluster

Photoinduced dynamics in an exchange-coupled trinuclear iron cluster

Florian Liedy[a], Rui Shi[b], Marco Coletta[a], Julia Vallejo[a], Euan K. Brechin[a], Georgios Lefkidis[b,c,*], Wolfgang Hübner[b], J. Olof Johansson[a,*]

[a] *EaStCHEM School of Chemistry, University of Edinburgh, David Brewster Road, EH9 3FJ, Edinburgh, UK*
[b] *Department of Physics and Research Center OPTIMAS, Technische Universität Kaiserslautern, Box 3049, 67653, Kaiserslautern, Germany*
[c] *School of Mechanics, Civil Engineering and Architecture, Northwestern Polytechnical University, Xi'an 710072, China*

Abstract

We present a joint experimental and computational study of the trinuclear basic carboxylate iron complex $Fe^{III}{}_2Fe^{II}O(CH_3CO_2)_6(H_2O)_3$, which is a model system for understanding photoinduced ultrafast spin dynamics in magnetic iron-based transition metal oxides. We have carried out femtosecond optical transient absorption spectroscopy of molecules in solution at room-temperature exciting either at 400 or 520 nm and observed a long-lived excited-state absorption (ESA) signal from ca. $400 - 670$ nm. The ESA signal is composed of several broad un-resolved bands at 405, 440 and 530 nm. The decay dynamics are complicated and three exponentials with corresponding decay time constants of $\tau_1 = 360 \pm 30$ fs, $\tau_2 = 5.3 \pm 0.6$ ps, $\tau_3 = 65 \pm 5$ ps and a constant offset ($\tau_4 > 500$ ps) were needed to fit the data over the full wavelength range. The data indicate that the lowest excited state is populated within the duration of the excitation pulse (< 120 fs). Highly correlated coupled-cluster calculations can satisfactorily reproduce the experimental vibrational spectrum and highlight the role of the μ_3-oxo bridge connecting the Fe ions to create a highly correlated ground-state and identify the excited state as having a mixture of both charge-transfer and ligand-field/d-orbital characters.

Keywords: Nanomagnetism, molecular magnetism, ultrafast dynamics, iron oxide complexes, quantum chemistry
2019 MSC: 00-01, 99-00

1. Introduction

Since the discovery of laser-induced ultrafast magnetization dynamics on ferromagnetic Ni [1], immense progress has been achieved in the field of nanospintronics, in which the electronic spin rather than the charge is used as the computational information carrier [2, 3]. One basic aspect of such approaches, is that the magnetic centres of the studied structures are different enough to be distinguishable (leading to spin localization), but not too different, so that there is still enough electronic overlap between them to allow for spin transfer. It has been predicted that ultrafast laser-induced spin-flip Λ–processes can shift local spin density from one site to another in a magnetic molecule [4–7]. In the present study, we take advantage of the mixed valency in the basic carboxylate tri-nuclear iron complex $Fe^{III}{}_2Fe^{II}O(CH_3COO)_6(H_2O)_3$ (Figure 1), or "Fe_3", which slightly breaks the trigonal symmetry [8]. Fe_3 is an interesting system to study spin transfer because of the μ_3–oxo bridge (labelled O_6 in Figure 1), which, together with the six carboxylates, connects the three ions together and provides exchange pathways, with different values reported in the literature ranging from approximately $J = -50$ to -10 cm^{-1} (based on the $-2J$ formalism) [8, 9]. The coupling between electrons, spins and vibrational (lattice) motion in the photoexcited state in these highly-correlated molecules, is not well understood and is a problem that underpins many ultrafast processes in magnetic solid-state systems.

*Corresponding authors
Email addresses: lefkidis@physik.uni-kl.de (Georgios Lefkidis), olof.johansson@ed.ac.uk (J. Olof Johansson)

Fe_3 is a mixed-valence complex with one Fe(II) ion (electron configuration $t_{2g}^4 e_g^2$) and two Fe(III) ions (electron configuration $t_{2g}^3 e_g^2$) [8], where all iron ions are in the high-spin state. In fact, one of the reasons to choose this particular cluster for possible subsequent dynamics investigations is exactly this: the ability to have similar but not identical magnetic centres. The binding motif of all three ions is a distorted octahedron due to different ligands. The μ_3–oxo bridge leads to a delocalization of electron density from the Fe(II) at room temperature and all three μ_3O–Fe bonds are almost equal in length [10]. It has been reported that the electron transfer time between the iron sites is 2.5 ns at room temperature [9]. For the femtosecond optical transient absorption (fs-OTA) measurements presented here, the electronic configuration can therefore be seen as a localised mixed-valence state. In the context of ultrafast magnetism, one interesting observation is that spin-forbidden ligand-field transitions (metal-centred $d-d$ transitions) become allowed due to the exchange-coupling between the ions in the trinuclear complex [11]. Indeed, the electronic spectra in the visible and NIR region of Fe_3 and the cation Fe_3^+ (containing only Fe(III) ions), are dominated by ligand-field transitions observed in Fe(III) monomers, but with significantly enhanced oscillator strength [11].

In simpler Fe(III) monomers, spin-flips via intersystem crossing (ISC) are known to happen on ultrafast timescales. For example, it has been shown in $Fe(acac)_3$ that charge-transfer (CT) excitation leads to population of the lowest excited ligand-field state, corresponding to a change from $S = 5/2$ to $S = 3/2$ within < 400 fs [12]. Ultrafast ISC is known to happen in other systems, such as the well-studied Fe(II) spin-crossover compounds where the $S = 0$ to $S = 2$ transition happens in less than 200 fs [13–16], in $Cr(acac)_3$ [17, 18], and in thin films of Cr(III) molecule-based magnets[19, 20].In transition metal complexes, multiple electronic potential energy surfaces intersect at high energies above the ground state due to the large density of states. The excited states are usually associated with a large change in geometry, meaning that there is a fast motion out of the Franck-Condon region along the steep potential energy surface towards the minimum of the excited state potential, which is why the change in spin can occur so quickly. Studies on Fe(III) trimers have been carried out by Hanna *et al.* [21]. They used fs-OTA spectroscopy to study $[Fe^{III}{}_3O(O_2CPh)_6(C_5H_5N)_3]ClO_4$ (Ph = phenyl), or "$Fe(III)_3$–BzPy", and found that photoexcitation results in population of a long-lived CT state with a lifetime on the order of 250 ps. We recently carried out a study on a trinuclear complex containing three Mn(III) ions bridged by μ_3–oxo and oxime bridges. We found that the lowest excited state corresponds to a shift from axial to equatorial Jahn-Teller distortion and that the fast motion out of the Franck-Condon region after photoexcitation took place via the formation of a coherent vibrational wavepacket. However, due to the μ_3–oxo and oxime bridges, the motion of the wavepacket was constrained along the axial Jahn-Teller axis, leading to a simple reaction coordinate but a much shorter excited-state lifetime of 9 ps [22], which is considerably shorter than what Hanna *et al.* observed for the Fe(III) trimer [21].

Here, we present a joint experimental and computational study of Fe_3 to understand its ultrafast photophysics. We have carried out fs-OTA of the molecules in solution and interpret the results using quantum chemical calculations to identify the excited states involved in the process. We found that regardless of excitation wavelength (400 and 520 nm), an excited state with charge-transfer and ligand-field character is populated within 120 fs and lives for more than 500 ps.

2. Experimental and computational methods

2.1. Transient absorption

The fs-OTA setup is based on the one presented in Ref. [23]. The pump pulse of wavelength λ_p was either the second harmonic ($\lambda_p = 400$ nm) of the output from a Coherent Legend Elite laser (pulse duration 120 fs) or the output from a commercial noncollinear optical parametric amplifier (NOPA) (TOPAS White from Light Conversion, pulse duration 50 fs and output set to $\lambda_p = 520$ nm). The pump pulses were focused into the sample by a $f = 500$ mm concave mirror producing a spot size ($1/e^2$) of 163 μm for $\lambda_p = 400$ nm and 360 μm for $\lambda_p = 520$ nm. The laser fluence was 4.07 mJ/cm^2 for $\lambda_p = 400$ nm and 1.48 mJ/cm^2 for $\lambda_p = 520$ nm. A broadband white light continuum was produced by focusing 1.4 μJ/pulse of the 800 nm fundamental with an f = 100 mm fused silica lens in a 5 mm thick CaF_2 plate, which was continuously moved in two dimensions. The white light was collimated with an

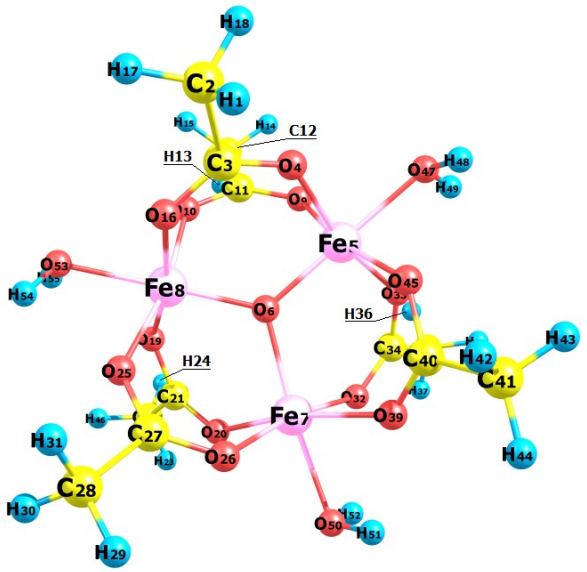

Figure 1: Theoretically optimized $Fe_3O(CH_3CO_2)_6(H_2O)_3$ structure at the HF level for the triplet ground state using the 3-21G basis set. The central μ_3–oxo–bridge in the centre of the molecule connects the three iron ions and provides an exchange pathway along with the six carboxylate ligands. Colour code: oxygen, red; iron, pink; carbon, yellow; hydrogen, blue.

$f = 100$ mm concave mirror and the 800 nm fundamental was removed with a dielectric filter. The detected probe spectrum spanned $320 \leq \lambda \leq 720$ nm. The white light beam was divided into a probe and reference beam using a reflective metallic neutral density filter. The probe light was focused into the sample with an $f = 500$ mm concave mirror. The probe beam diameter in the sample was 112 μm. The pump-probe polarization angle θ_{pp} was set to $\theta_{pp} = 54.7°$ (magic angle) to avoid anisotropic signals.

The time delay t between pump and probe was controlled by a delay stage and a retroreflector. For each time delay, 1000 spectra were collected. The whole procedure was repeated four times for $\lambda_p = 400$ nm and 16 times for $\lambda_p = 520$ nm to get 4000 and 16000 spectra in total for each delay position. The white-light beams were dispersed by two prisms and focused onto two fast CCD cameras from Entwicklungsbuero Stresing equipped with Hamamatsu S7031-0906 sensors with 512×58 active pixels. Full binning was used, where the 58 vertical pixel were binned, which allowed a synchronous read-out at 1 kHz for both probe and reference beams. The temporal resolution was determined from the cross-phase modulation in the solvent, giving values of 140 fs at $\lambda = 350$ nm and 90 fs for $500 \leq \lambda \leq 650$ nm for $\lambda_p = 520$ nm. For $\lambda_p = 400$ nm, the corresponding values were 180 fs at $\lambda = 350$ nm and 160 fs for $500 \leq \lambda \leq 650$ nm.

2.2. Materials

The samples were synthesised following Ref. [24]. Different concentrations were used for the different pump wavelengths due to difference in absorption at $\lambda = 400$ and 520 nm. The Fe_3 complex was dissolved in double-distilled water and the concentrations were 6.53 and 12.0 mM for $\lambda_p = 400$ nm and $\lambda_p = 520$ nm, respectively. A 200 μm pathlength flow-cuvette with a flow rate of 5 μL/min was used.

For the low-temperature measurements, the sample was dispersed in a thin polymer film made from poly(methyl methacrylate) (PMMA). For this, 0.52 g of PMMA (350,000 g/mol) was dissolved in 6 ml tetrahydrofuran (THF). 0.9 mg of the Fe_3 sample (627.88 g/mol) was subsequently dissolved under stirring in 3 ml PMMA/THF solution. The solution of PMMA and Fe_3 sample in THF was then poured into a 80 mm diameter glass petri dish for drying. A 50 mm inner diameter copper ring was used as a mould. The petri dish was covered with a large glass bowl to guarantee an even film surface. After drying, the film was removed under gentle heating. The samples were mounted in a Oxford Instruments continuous-flow cryostat (MicrostatHe-R).

2.3. Computational methods

The quantum mechanical calculations were performed using the coupled-cluster method with single and double virtual excitations (CCSD) for the ground electronic state and the equation-of-motion coupled-cluster method with single and double virtual excitations (EOM-CCSD) for the excited electronic states as incorporated in the freely available GAMESS quantum chemical package [25, 26]. We used the 3-21G basis set, which although small, gave results which were very close to the experimental ones.

3. Results and discussion

3.1. Static electronic absorption spectrum

Figure 2 shows the electronic absorption spectrum of Fe_3 in water, which is in good agree-

ment with the literature [9]. The lowest energy transition observed occurs at 930 nm, which has been magnified in Figure 2 because of the low extinction coefficient. This transition has previously been assigned in Fe(III) oxo-bridged dimers to the spin-forbidden $^6A_1 \rightarrow {}^4T_{1,2}$ transition observed in monomeric Fe(III) [27]. Just like in the dimer, spin-forbidden transitions become allowed in the trimer because of coupling of the $^4T_{1,2}$ excited states with the ^6A ground state on the other ion in the molecule [27], which leads to increased oscillator strength. The visible spectrum is dominated by the tail of strong charge-transfer transitions in the UV ($\epsilon > 1000$ L mol^{-1} cm^{-1}). The shoulder at 480 nm has previously been assigned in the oxo-bridged dimer to a mixture of oxo $\rightarrow$ Fe(III) CT and ligand-field excitation [27]. These low-energy transitions are observed because of the covalent nature of the μ–oxo bonds, which leads to mixing of CT and ligand-field states [27]. Otherwise no peaks or further shoulders are observed and the extinction coefficient grows towards shorter wavelengths.

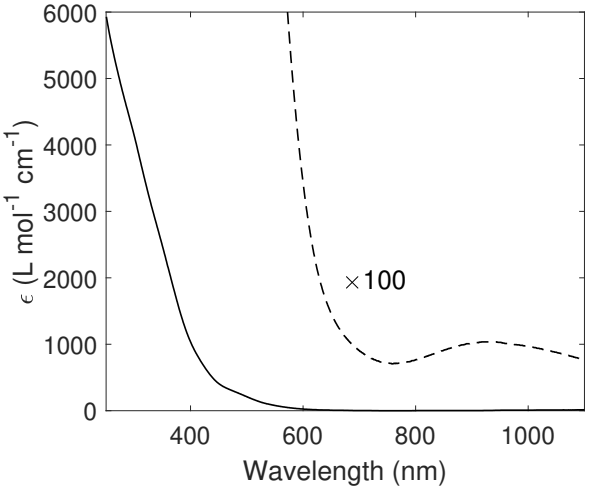

Figure 2: Electronic absorption spectrum of Fe_3 in water. The extinction coefficients $\epsilon(\lambda)$ in the NIR have been magnified and the lowest-energy transition at $\lambda = 930$ nm.

In the electronic structure calculations, altogether eight singlet and eight triplet states were found in the region up to about 3.5 eV (Table 1). From a theoretical point of view, the d-character of the molecular orbitals (MOs) on the iron sites is qualitatively evident by inspection of the MOs 149, 151, 152, and 154 (Figure 3), which are involved in the main virtual transitions 142 $\rightarrow$ 152, 149 $\rightarrow$ 154, 151 $\rightarrow$ 152, and 151 $\rightarrow$ 154 of the correlated CCSD many-body function, with transition amplitudes 0.231, 0.115, 0.234, and 0.189, respectively. In Figure 3, the electron delocalisation provided by the μ_3–oxo bridge is clearly seen by the electron density on the central μ_3O atom. The energies of the low-lying states 3 and 4 (Table 1), coincide with the OH stretch-modes of the water ligands and so it is difficult to analyse further. Transitions to states 5 – 7 (867 – 933 nm) agree very well with the peak in the absorption spectrum at 930 nm. The transition to state 8 at $\lambda = 630$ nm coincide with the sharp increase in oscillator strength seen in Figure 2. Of course, the peaks at lower energies do not correspond to a single electronic state, but are probably a combination of several electronic states with additional coupling to vibrational modes. Furthermore, solvent effects are neglected in the theoretical calculations, which, in principle, can shift transitions energies. Nevertheless, from Figure 3, it is clear that the excitations involve a simultaneous shift in electron density on several iron sites and the bridging oxygen atom, which results in increased oscillator strength of the spin-forbidden transitions. This is in agreement with results from the oxo-bridged dimers [27], where transitions in this wavelength region were assigned to a mixture of charge-transfer and ligand-field excitations.

Table 1: EOM-CCSD and CCSD energies and multiplicities of the lowest 9 many-body electronic excited states before the inclusion of SOC and an external static magnetic field $B = 10^{-5}$ a.u. These results use the HF level for the triplet ground state and the 3-21G basis set as a starting point.

State	Multiplicity	Energy (eV)
9	3	3.216
8	3	1.958
7	1	1.430
6	3	1.398
5	1	1.329
4	1	0.373
3	3	0.306
2	1	0.007
1	3	0.000

3.2. Femtosecond optical transient absorption spectroscopy

In Figure 4, the fs-OTA spectra $\Delta A(\lambda, t)$ for several pump-probe delays t after exciting at $\lambda_p =$

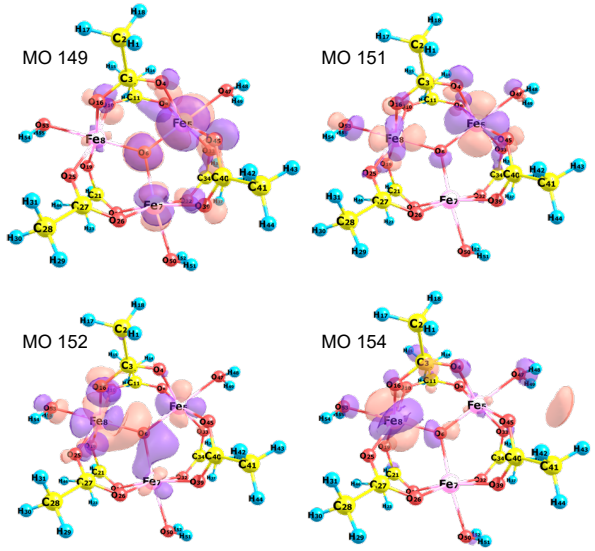

Figure 3: Molecular orbitals (MOs) involved in the main virtual transition 149 → 152, 149 → 154, 151 → 152, and 151 → 154 of the correlated CCSD many-body function (first excited state, which is also the reference state), with transition amplitudes 0.231, 0.115, 0.234, and 0.189, respectively. In order to enhance visibility of the orbitals, the structure is rotated with respect to Figure 1. Colour code: oxygen, red; iron, pink; carbon, yellow; hydrogen, blue.

400 and 500 nm are presented. The noisy signals around the excitation wavelengths are due to scattered pump light. The fs-OTA spectra are dominated by excited-state absorption (ESA) from ca. 400 − 670 nm. By exciting at different wavelengths, we observe that the ESA signal is composed of several broad unresolved bands at 405 nm (not observed for $\lambda_p = 400$ nm), 440 nm and 530 nm (not observed for $\lambda_p = 520$ nm). Below 400 nm, a steep drop in absorbance is observed, which could be due to overlap of ESA with the ground-state bleach (GSB). The spectrally broad ESA observed here is similar to the findings for the Fe(III) trimer $Fe(III)_3$–BzPy by Hanna *et al.* [21]. Due to a smaller spectral bandwidth of the white-light probe used in their study, only the shoulder at 530 nm was observed. In Figure 4, the peak structure of the ESA is still discernible after 38.4 ps and the ESA reaches a plateau at $t > 80$ ps. We have carried out a measurement up to $t = 500$ ps using $\lambda_p = 400$ nm (data not shown), in which the plateau is still observed and so the lifetime of the excited state is longer than 500 ps. As previously mentioned, a long-lived component was also observed for $Fe(III)_3$–BzPy [21].

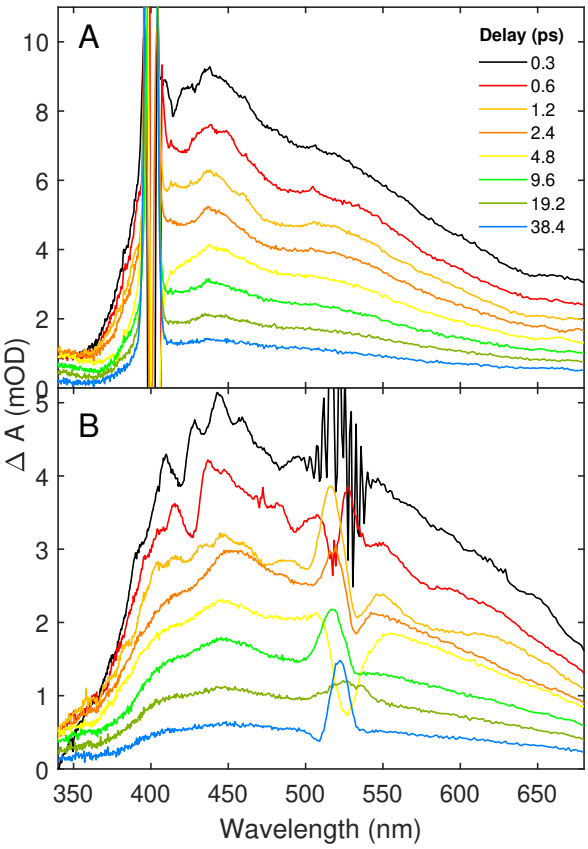

Figure 4: Femtosecond optical transient absorption spectra of Fe_3 in water at selected time delays after exciting at **A** $\lambda_p = 400$ nm and **B** $\lambda_p = 520$ nm. The noise around $\lambda = 400$ nm in **A** and 520 nm in **B** is due to scattered pump light.

For a better understanding of the decay kinetics, Figure 5 shows the kinetic traces at probe wavelength $\lambda = 440$ nm obtained from the fs-OTA data presented in Figure 4. It is clear that the ESA signal decays with multi-exponential kinetics and so we carried out a global analysis using the software package Glotaran [28]. The fs-OTA spectra $\Delta A(\lambda, t)$ are fitted with a sum of exponential functions, minimising the number of decay constants using a singular value decomposition method according to

$$\Delta A(\lambda, t) = \sum_{i=1}^{n_{\text{comp}}} c_i(\lambda) \exp\left(-\frac{t}{\tau_i}\right), \qquad (1)$$

where n_{comp} is the number of components and the amplitude $c_i(\lambda)$ is the fitted decay-associated spec-

trum (DAS) for the i'th decay constant τ_i. The global analysis takes into account the instrument response function and the cross-phase modulation from the solvent. We found that three decay constants and a constant offset (to capture the plateau) were needed to fit the data. The fit parameters are presented in Table 2 and the corresponding DAS in Figure 6. The quality of the fit can be seen for $\lambda = 440$ nm in Figure 5. We note that the value of τ_3 is on the order of the longest time-delay. The aforementioned measurement up to $t = 500$ ps (using $\lambda_p = 400$ nm), resulted in $\tau_3 = 31 \pm 0.4$ ps, which is half of the value of τ_3 presented in Table 2 for $\lambda_p = 400$ nm. To obtain a more reliable value, even longer t are needed. However, the longer decay-dynamics and the exact value of τ_3 is not the main point of this study and we conclude that there is a decay channel with a time constant on the order of tens of picoseconds and one with a time constant much longer than 500 ps. The key observation is that a long-lived state is populated. We finish the discussion on the decay kinetics by also mentioning that we have carried out measurements at low temperatures to investigate any potential influence on the dynamics of different exchange-coupled states populated at higher temperatures (note that $J = -50$ cm^{-1} corresponds to *ca.* 70 K). The results are shown in Figure 7, where the two ESA peaks at 440 and 530 nm can be seen. The extracted time constants were smaller than the room-temperature measurements in water, but consistent across all temperatures measured. The average values over the temperature range $77 \leq T \leq 280$ K were $< \tau_1 >_{\text{lowT}} = 232 \pm 12$ fs, $< \tau_2 >_{\text{lowT}} = 5.0 \pm 0.4$ ps, and $< \tau_3 >_{\text{lowT}} = 67 \pm 3$ ps.

Table 2: Fitted decay constants τ_i extracted from the global analysis (Equation 1). The corresponding amplitudes are shown in the DAS in Figure 6.

λ_p (nm)	τ_1(fs)	τ_2(ps)	τ_3(ps)
400	360 ± 30	5.3 ± 0.6	65 ± 5
520	460 ± 40	8.9 ± 2	88 ± 12

We make the following key observations from the fs-OTA measurements described above. The spectral shape of the fs-OTA spectra in Figure 4 do not change over time delays ranging from *ca.* 200 fs to over 500 ps. This implies that there is no change in electronic character after the initial excitation [17]. It is possible that there is a change in electronic state on a sub-100 fs timescale, which we cannot resolve with our experimental temporal resolution. On the other hand, exciting at $\lambda_p = 400$ or 520 nm results in the same fs-OTA spectra, which implies that whatever happens during the first 100 fs, a long-lived state with lifetime over 500 ps is populated. It is likely that the energy of the state has to be on the order of ∼eV above the ground state because of the long lifetime. The state is non-emissive (data not shown), which indicates that it is not a pure CT state (as was recently discovered in the low-spin Fe(III) monomer $[Fe(btz)_3]^{3+}$ [29]). These observations lead us to conclude that the lowest excited ligand-field/CT state is populated within 120 fs. This state should be partly delocalised because of the broad ESA signal across the whole visible spectrum. This is also verified by the calculations, which identify a ligand-field/CT excited state, involving MOs 151 → 154 (Figure 3), with electron density also over the μ_3–oxo bridge. Because of the large spin angular momenta on the ions, it is not straightforward to identify ISC processes, as in spin-crossover in Fe(II) monomers. On

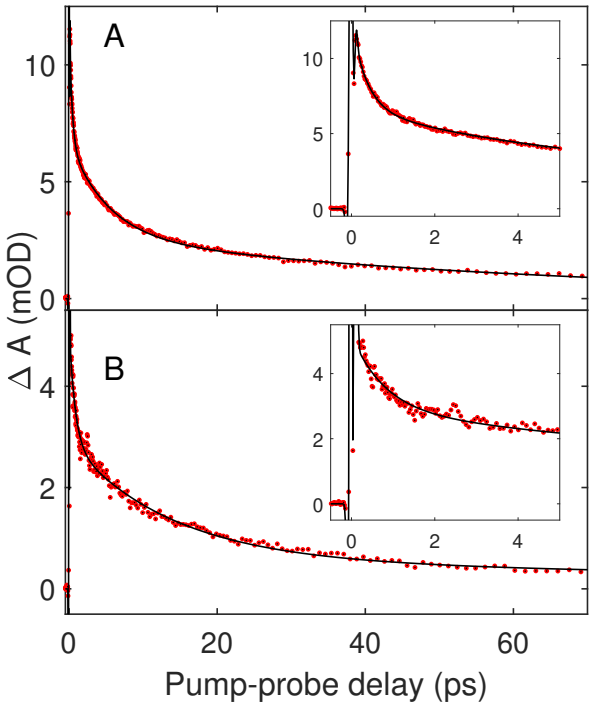

Figure 5: Kinetic traces at $\lambda = 440$ nm extracted from the data in Figure 4 after exciting Fe_3 in water at **A** $\lambda_p = 400$ nm and **B** $\lambda_p = 520$ nm. The insets show the dynamics for time delays $t \leq 5$ ps. The red dots are experimental data points and the black lines are the fits from the global analysis.

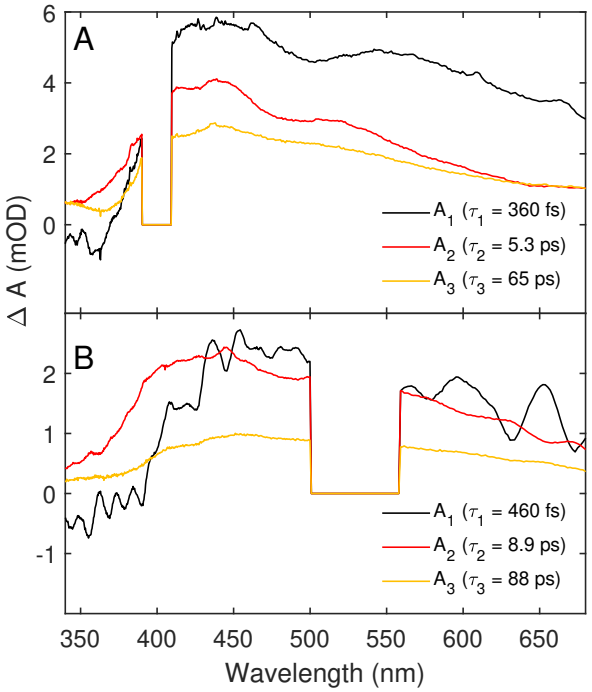

Figure 6: Decay-associated spectra (DAS) from the global analysis (Equation 1). The DAS for $\lambda_p = 400$ nm are shown in **A** and $\lambda_p = 520$ nm in **B**. The spectral region around λ_p was excluded from the fits. The scattered pump light at 400 nm (A) and 520 nm (B) have been removed from the fit procedure using a step function.

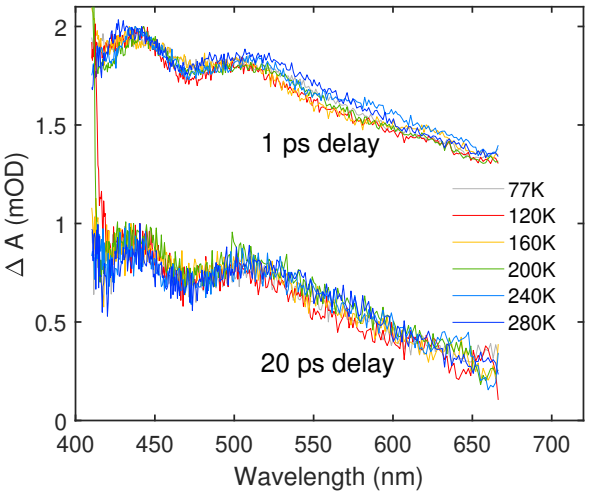

Figure 7: Temperature-dependent fs-OTA measurements after exciting with $\lambda_p = 400$ nm, measured on Fe_3 dispersed in a PMMA film. The difference spectra for 1 ps and 20 ps pump-probe delay for temperatures from 77 K to 280 K are shown.

the other hand, the coupled-cluster calculations allow for more insights, where the effect of spin-orbit coupling (SOC) is accounted for through the calculation of the one-electron SOC-integrals and the use of effective core potentials for the contributions for the two-electron integrals [30, 31], a combination which has proven to give very good results for the first-row transition elements [32]. Table 3 shows the energies after the inclusion of SOC and a static external magnetic field of magnitude $B = 10^{-5}$ a.u., which serves to numerically distinguish between the spin-up and the spin-down states (Zeeman splitting). The spin-density localization is calculated with a gross population analysis of the one-electron reduced-density matrix of each many-body electronic state [33]. As can be seen in Table 3, a range of different spin densities is observed in the energy range of the lowest excited ligand-field manifold (states 9 - 11).

3.3. Vibrational modes and electron correlations

It has already been shown that molecular vibrations can play a very significant role regarding the correlational and heat content of magnetic molecules [34–37]. Therefore, it is imperative to study the behaviour of magnetic molecules with respect to their vibrational spectra, especially when aiming at room-temperature operating conditions. In Figure 8 the FT-IR spectrum of the Fe_3 powder is shown. The spectrum was measured using the ATR mode of an FT-IR spectrometer. The spectrum fits very well to the literature spectrum [9]. We see a broad water OH-stretch peak with a maximum at 3400 cm^{-1} with two shoulders at 3550 cm^{-1} and 3190 cm^{-1}. Further there are two weak peaks at 2982 cm^{-1} and 2940 cm^{-1}, corresponding to the aliphatic CH stretch-modes. The modes between 1350-1590 cm^{-1} are assigned as C–O–Fe stretch modes.

The vibrational spectrum is calculated in the following way. First at the Hartree-Fock level theory (both for a triplet and a singlet ground state), for which analytical derivatives of the total energy with respect to the dislocations are available, we calculate the force matrix, and hence the altogether normal modes and their respective vibrational frequencies (Table 4). Then for selected normal modes, we calculate energy snapshots at the EOM-CCSD level for eleven (in some cases thirteen) points along

Table 3: EOM-CCSD energies and localised spin densities of the lowest 19 many-body electronic states after the inclusion of SOC and an external magnetic field $B = 10^{-5}$ a.u. For the numbering of the iron atoms, see Figure 1. These results use the HF level for the triplet ground state and the 3-21G basis set as starting point.

State	Energy (eV)	Fe5	Fe7	Fe8
19	3.355	0.343	0.343	0.413
18	3.354	0.041	0.042	0.051
17	3.353	-0.384	-0.386	-0.463
16	2.100	0.304	0.055	0.360
15	2.098	0.824	0.145	0.979
14	2.097	-1.129	-0.196	-1.334
13	1.595	0.005	-0.010	0.001
12	1.536	0.416	0.044	0.136
11	1.535	-0.395	-0.042	-0.130
10	1.507	-0.023	0.008	-0.007
9	1.465	-0.001	0.002	-0.000
8	0.537	-0.003	-0.001	-0.000
7	0.495	0.039	-0.008	0.009
6	0.445	0.037	0.013	0.021
5	0.443	-0.056	-0.022	-0.030
4	0.201	-0.009	0.009	0.006
3	0.132	0.003	-0.000	-0.001
2	0.130	-0.004	-0.001	-0.000
1	0.000	-0.007	0.007	-0.004

the normal mode and fit the total-energy curve to a quadratic and a cubic polynomial [38]. A scaling factor of 0.943 is used [39]. The results for some characteristic modes are summarized in Table 4. There are some general trends. Generally, the EOM-CCSD-based vibrational frequencies can differ substantially from the HF-based ones. The reason for this is that for some modes (notably the ones including a drastic change in the Fe-Fe interatomic distances) the total energy strongly depends on the static correlational content of the electronic many-body state. Thus, in highly correlated states, a small change in the Fe−Fe distance can have a large effect on the total energy. Although this usually leads to lower vibrational frequencies than HF-based ones (e.g., mode 140) in some cases it can also go in the opposite direction (e.g., notably for modes 162 and 164). This makes it imperative to consider post-HF methods for the vibrational spectrum of such highly-correlated magnetic molecules, even for the ground electronic state, since correlations can in some cases shift the IR absorption frequencies by a few hundred cm^{-1}. A further consequence of this fact is that the quality of the correlation can generally change the vibrational frequency, even for the same number of points. As an extreme example, we mention that for normal mode 141 if we decrease the active window from 80 to 70 (i.e., include 35 occupied and 35 empty molecular orbitals for the EOM-CCSD calculation, instead of 40 occupied and 40 empty ones) the vibrational frequency increases from 1714.69 to 1866.85 cm^{-1}. However, this active window does not correctly include all molecular orbitals participating in the virtual excitations, thus leading to rather questionable results. Furthermore, starting from a triplet rather than a singlet ground state for the preliminary HF calculation also shifts the frequencies (e.g., for normal mode 110, the HF frequency becomes 1525.93 cm^{-1}, and the two CCSD frequencies (for quadratic and cubic polynomial fitting respectively), are shifted from 1437.02 to 1498.87 cm^{-1}, and from 1445.38 to 1495.68 cm^{-1}, respectively.

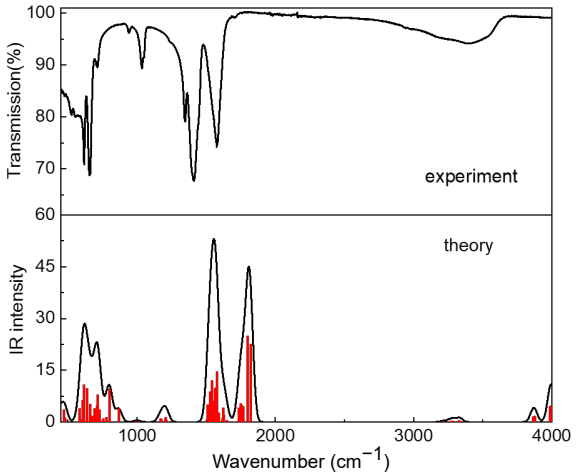

Figure 8: Fe_3 experimental FT-IR ATR vibrational spectrum obtained on a powder sample (top) and theoretical (bottom) vibrational spectrum at the HF level (for triplet ground state). For the frequency of selected normal modes at the EOM-CCSD level see Table 4. The theoretical spectrum is also presented with a Gaussian broadening of 54 cm^{-1} (full width at half maximum) as a solid black line in the lower panel.

4. Conclusions

In conclusion, we have carried out femtosecond optical transient absorption spectroscopy and high-level quantum chemistry calculations of

Table 4: Frequencies of selected vibrational modes at different theory levels (see text). For the correlations an active window of 80 molecular orbitals is used (40 occupied and 40 empty ones). The results of this table are based on a singlet HF ground state.

Normal mode	Number of points	HF frequency (cm^{-1})	CCSD frequency (cm^{-1}) (quadratic polynomial)	CCSD frequency (cm^{-1}) (cubic polynomial)
87	11	739.47	774.84	816.28
96	13	1081.65	950.25	932.01
110	11	1493.82	1437.02	1445.38
111	11	1498.84	1398.72	1392.21
140	11	1800.14	1550.57	1677.11
141	11	1812.51	1714.69	1714.69
162	11	3873.84	3927.33	3834.08
164	11	3971.23	4007.50	4007.50
165	11	4013.54	3816.38	3817.39

$Fe^{III}{}_2Fe^{II}O(CH_3CO_2)_6(H_2O)_3$, or "$Fe_3$", in order to understand the excited state dynamics after photoexcitation. The lowest charge-transfer/ligand-field excited state, ca. 1.5 eV above the ground state, was populated within < 120 fs and corresponds to a delocalised state with ligand-field excitation at several iron sites and delocalised over the μ_3–oxo bridge. The initial dynamics over the first tens of ps could be described with a multi-exponential decay, but a remaining population of this state lived for more than 500 ps. These results open up possibilities to further study spin-switching Λ–processes in these interesting exchange-coupled polynuclear metal oxide clusters.

Acknowledgements

JOJ and FL thank the Royal Society of Edinburgh and the Carnegie Trust (Collaborative Research Grant) for funding. EKB thanks the EPSRC for grants EP/P025986/1 and EP/N01331X/1.

References

References

[1] E. Beaurepaire, J.-C. Merle, A. Daunois, J.-Y. Bigot, Physical review letters 76 (1996) 4250–4253.

[2] S. Saha, S. Barman, Y. Otani, A. Barman, Nanoscale 7 (2015) 18312–18319. doi:10.1039/C5NR05634A.

[3] S. Mangin, M. Gottwald, C.-H. Lambert, D. Steil, V. Uhlíř, L. Pang, M. Hehn, S. Alebrand, M. Cinchetti, G. Malinowski, Y. Fainman, M. Aeschlimann, E. E. Fullerton, Nature materials 13 (2014) 286–92. doi:10.1038/nmat3864.

[4] G. Lefkidis, W. Hübner, Physical Review B 87 (2013) 014404. doi:10.1103/PhysRevB.87.014404.

[5] C. Li, S. Zhang, W. Jin, H. Xiang, G. Lefkidis, W. Hübner, Journal of Magnetism and Magnetic Materials 324 (2012) 4024–4029. doi:10.1016/j.jmmm.2012.07.007.

[6] W. Jin, F. Rupp, K. Chevalier, M. M. N. Wolf, M. C. Rojas, G. Lefkidis, H.-J. Krüger, R. Diller, W. Hübner, Physical Review Letters 109 (2012) 267209. doi:10.1103/PhysRevLett.109.267209.

[7] W. Jin, C. Li, G. Lefkidis, W. Hübner, Physical Review B 89 (2014) 024419. doi:10.1103/PhysRevB.89.024419.

[8] R. D. Cannon, R. P. White, Progress in Inorganic Chemistry 36 (1988) 196 – 298. doi:10.1002/9780470166376.ch3.

[9] C. T. Dziobkowski, J. T. Wrobleski, D. B. Brown, Inorganic Chemistry 20 (1981) 679–684. doi:10.1021/ic50217a008.

[10] T. Sato, F. Ambe, K. Endo, M. Katada, H. Maeda, T. Nakamoto, H. Sano, Journal of the American Chemical Society 118 (1996) 3450–3458. doi:10.1021/ja953038y.

[11] P. J. McCarthy, H. U. Güdel, Coordination Chemistry Reviews 88 (1988) 69–131. doi:10.1016/0010-8545(88)80002-X.

[12] E. M. S. Maçôas, R. Kananavicius, P. Myllyperkiö, M. Pettersson, H. Kunttu, The Journal of Physical Chemistry A 111 (2007) 2054–2061. doi:10.1021/jp066271z.

[13] J. E. Monat, J. K. McCusker, Journal of the American Chemical Society 122 (2000) 4092–4097. doi:10.1021/ja992436o.

[14] G. Auböck, M. Chergui, Nature Chemistry 7 (2015) 629–633. doi:10.1038/nchem.2305.

[15] H. T. Lemke, K. S. Kjær, R. Hartsock, T. B. van Driel, M. Chollet, J. M. Glownia, S. Song, D. Zhu, E. Pace, S. F. Matar, M. M. Nielsen, M. Benfatto, K. J. Gaffney, E. Collet, M. Cammarata, Nature Communications 8 (2017) 15342. doi:10.1038/ncomms15342.

[16] S. Zerdane, L. Wilbraham, M. Cammarata, O. Iasco, E. Rivière, M. L. Boillot, I. Ciofini, E. Collet, Chemical Science 8 (2017) 4978–4986. doi:10.1039/c6sc05624e.

[17] E. A. Juban, J. K. McCusker, Journal of the American Chemical Society 127 (2005) 6857–6865. doi:10.1021/ja042153i.

[18] J. N. Schrauben, K. L. Dillman, W. F. Beck, J. K. Mc-

Cusker, Chemical Science 1 (2010) 405. doi:10.1039/c0sc00262c.
[19] J. O. Johansson, J.-W. Kim, E. Allwright, D. M. Rogers, N. Robertson, J.-Y. Bigot, Chem. Sci. 7 (2016) 7061–7067. doi:10.1039/C6SC01105E.
[20] L. Hedley, M. D. Horbury, F. Liedy, J. O. Johansson, Chemical Physics Letters 687 (2017) 125–130. doi:10.1016/j.cplett.2017.08.070.
[21] L. Hanna, P. Kucheryavy, C. Liu, X. Zhang, J. V. Lockard, Journal of Physical Chemistry C 121 (2017) 13570–13576. doi:10.1021/acs.jpcc.7b03936.
[22] F. Liedy, R. McNab, J. Eng, R. Inglis, T. Penfold, E. K. Brechin, J. O. Johansson, ChemRxiv (2019). doi:10.26434/chemrxiv.7485011.v1.
[23] U. Megerle, I. Pugliesi, C. Schriever, C. F. Sailer, E. Riedle, Applied Physics B: Lasers and Optics 96 (2009) 215–231. doi:10.1007/s00340-009-3610-0.
[24] A. B. Blake, A. Yavari, W. E. Hatfield, C. N. Sethulekshmi, Journal of the Chemical Society, Dalton Transactions (1985) 2509. doi:10.1039/dt9850002509.
[25] J. R. Gour, P. Piecuch, M. Włoch, The Journal of Chemical Physics 123 (2005) 134113. doi:10.1063/1.2042452.
[26] M. W. Schmidt, K. K. Baldridge, J. A. Boatz, S. T. Elbert, M. S. Gordon, J. H. Jensen, S. Koseki, N. Matsunaga, K. A. Nguyen, S. Su, T. L. Windus, M. Dupuis, J. A. Montgomery, Journal of Computational Chemistry 14 (1993) 1347–1363. doi:10.1002/jcc.540141112.
[27] F. Tuczek, Coordination Chemistry Reviews 219-221 (2001) 1075–1112. doi:10.1016/S0010-8545(01)00382-4.
[28] J. J. Snellenburg, S. P. Laptenok, R. Seger, K. M. Mullen, I. H. M. van Stokkum, Journal of Statistical Software 49 (2012) 1–22. doi:10.18637/jss.v049.i03.
[29] P. Chábera, Y. Liu, O. Prakash, E. Thyrhaug, A. E. Nahhas, A. Honarfar, S. Essén, L. A. Fredin, T. C. B. Harlang, K. S. Kjær, K. Handrup, F. Ericson, H. Tatsuno, K. Morgan, J. Schnadt, L. Häggström, T. Ericsson, A. Sobkowiak, S. Lidin, P. Huang, S. Styring, J. Uhlig, J. Bendix, R. Lomoth, V. Sundström, P. Persson, K. Wärnmark, Nature 543 (2017) 695–699. doi:10.1038/nature21430.
[30] W. R. Wadt, P. J. Hay, The Journal of Chemical Physics 82 (1985) 284–298. doi:10.1063/1.448800.
[31] P. J. Hay, W. R. Wadt, The Journal of Chemical Physics 82 (1985) 299–310. doi:10.1063/1.448975.
[32] G. Lefkidis, W. Hübner, Physical Review Letters 95 (2005) 077401. doi:10.1103/PhysRevLett.95.077401.
[33] A. Szabo, N. S. Ostlund, Modern Quantum Chemistry, Dover Publications, Inc, New York, 1996.
[34] P. Moriarty, Y. Ma, M. Upward, P. Beton, Surface Science 407 (1998) 27–35. doi:10.1016/S0039-6028(98)00082-X.
[35] M. J. Butcher, F. H. Jones, P. Moriarty, P. H. Beton, K. Prassides, K. Kordatos, N. Tagmatarchis, Applied Physics Letters 75 (1999) 1074–1076. doi:10.1063/1.124601.
[36] C. D. Dong, G. Lefkidis, W. Hübner, Physical Review B 88 (2013) 214421. doi:10.1103/PhysRevB.88.214421.
[37] C. Li, J. Liu, S. Zhang, G. Lefkidis, W. Hübner, Carbon 87 (2015) 153–162. doi:10.1016/j.carbon.2015.02.016.
[38] D. Dutta, M. Becherer, D. Bellaire, F. Dietrich, M. Gerhards, G. Lefkidis, W. Hübner, Physical Review B 97 (2018) 224404. doi:10.1103/PhysRevB.97.224404.
[39] R. D. Johnson III, NIST Computational Chemistry Comparison and Benchmark Database, NIST Standard Reference Database Number 101, 2019.